

www.acsnano.org

Observing the Dynamics of an **Electrochemically Driven Active Material with Liquid Electron Microscopy**

Wyeth Gibson, Justin T. Mulvey, Swetamber Das, Serxho Selmani, Jovany G. Merham, Alexander M. Rakowski, Eric Schwartz, Allon I. Hochbaum, Zhibin Guan, Jason R. Green, and Joseph P. Patterson*



Downloaded via UNIV OF CALIFORNIA IRVINE on May 14, 2024 at 23:51:35 (UTC). See https://pubs.acs.org/sharingguidelines for options on how to legitimately share published articles.

Cite This: ACS Nano 2024, 18, 11898-11909



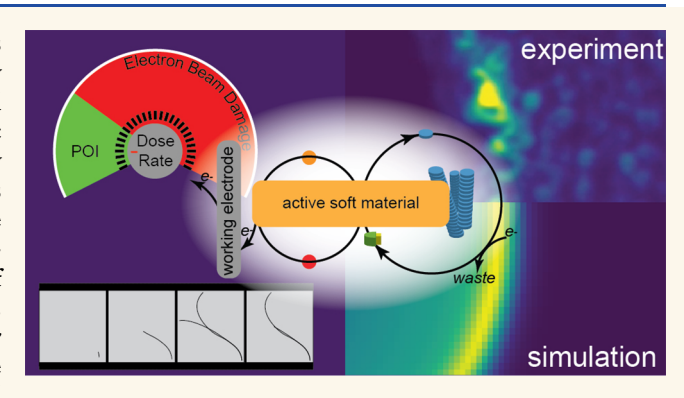
ACCESS

III Metrics & More

Article Recommendations

Supporting Information

ABSTRACT: Electrochemical liquid electron microscopy has revolutionized our understanding of nanomaterial dynamics by allowing for direct observation of their electrochemical production. This technique, primarily applied to inorganic materials, is now being used to explore the self-assembly dynamics of active molecular materials. Our study examines these dynamics across various scales, from the nanoscale behavior of individual fibers to the micrometer-scale hierarchical evolution of fiber clusters. To isolate the influences of the electron beam and electrical potential on material behavior, we conducted thorough beam-sample interaction analyses. Our findings reveal that the dynamics of these active materials at the nanoscale are shaped by their proximity to the electrode and



the applied electrical current. By integrating electron microscopy observations with reaction-diffusion simulations, we uncover that local structures and their formation history play a crucial role in determining assembly rates. This suggests that the emergence of nonequilibrium structures can locally accelerate further structural development, offering insights into the behavior of active materials under electrochemical conditions.

KEYWORDS: liquid EM, in situ electron microscopy, electrochemistry, active materials, molecular self-assembly

INTRODUCTION

Living active materials use competing chemical reaction systems to create complex and dynamic hierarchical structures. This results in a system in which the structural dynamics is very sensitive to the steady state established by these competing reactions. This sensitivity allows active materials to respond to changes in their environment and endows them with properties such as self-healing, homeostasis, and motility.^{2–4} A key feature of these systems is that they exist away from thermodynamic equilibrium, which is achieved through constant input and the dissipation of energy.

Synthetic systems have been developed in an attempt to mimic the reaction networks and dynamic behaviors of living active materials.^{1,5} These systems can be produced using chemical reactions, 1,6-8 light, 9-13 or electrochemical stimulus. $^{14-16}$ While enormous efforts have been made to understand the self-assembly mechanisms of living active materials, such as actin assembly, 17 there is currently a large knowledge gap on how these synthetic mimics behave. The transient and dynamic

nature of these materials presents challenges in characterization, as they require a constant supply of "fuel" and elimination of "waste" to maintain their active form. 18 Consequently, in situ analysis is necessary to fully comprehend active materials and how the layers of the hierarchical structure interplay. 19 Typically, electron microscopy is used to study the morphology of these materials, and optical microscopy is used to study their dynamics. 20-22 Traditional optical microscopy is diffractionlimited, regularly achieving resolutions of 250 nm, with reports of resolutions of 100 nm.²³ Super-resolution microscopy is a class of optical microscopy techniques that have surpassed the diffraction limit with reports of resolutions of 10 nm having been

Received: January 31, 2024 Revised: March 25, 2024 Accepted: April 4, 2024 Published: April 22, 2024





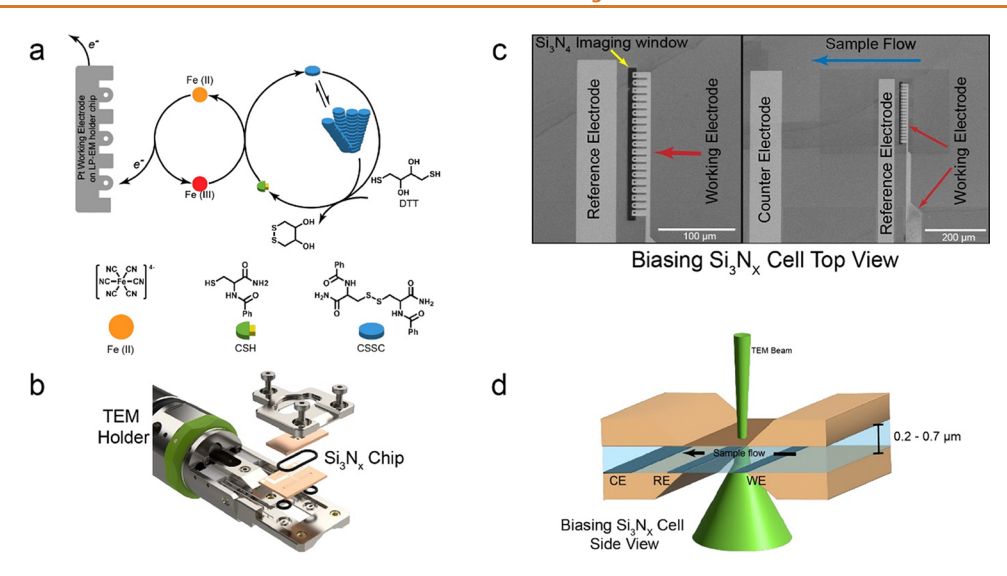


Figure 1. Overview of the reaction network and liquid EM holder. (a) Reaction network showing the process of electrochemical oxidation of ferrocyanide to ferricyanide, after which the ferrocyanide oxidizes CSH. Two oxidized CSH molecules then form CSSC which goes on to self-assemble into fibers. CSH is regenerated through the reduction of CSSC by DTT. This reduction causes disassembly of the self-assembled fibers. (b) Exploded diagram of the DENSsolutions Stream liquid-phase EM holder tip assembly. (c) Scanning electron micrographs showing all three electrodes in relation to one another with a zoomed-in view of the working electrode showing the comb-like topology. (d) Illustration of the silicon nitride liquid cell depicting the counter (CE), reference (RE), and working (WE) electrodes with sample flow direction and the TEM electron beam.

achieved.^{24,25} However, to get 10 nm resolution, the fluorescent emitters must be sparse having approximately 200 nm between each emitter.²⁶ Transmission electron microscopy (TEM) can obtain subangstrom resolutions. As the name implies, the TEM relies on the transmission of electrons through the sample. As a result, the resolution one can obtain is directly related to the thickness of the sample due to chromatic aberrations the sample imparts on the electron beam. Assuming the material has a low atomic number (Z < 30), typical resolutions are approximately 2 nm to 12 nm for a 200 nm to 1 μ m thick sample, respectively.^{27,28} Liquid electron microscopy (liquid EM) is a transformative technique that has made profound impacts in multiple fields of research.^{29–33} Liquid EM's value comes from its ability to provide high-resolution movies of samples in their native liquid state. Liquid EM does this by utilizing silicon nitride-coated silicon chips that have been processed to provide a strong ~50 nm electron transparent membrane between the EM column vacuum and the liquid sample. These membranes can be patterned with \sim 40 nm thick microelectrodes, giving the ability to perform electrochemical measurements during imaging. Imaging such material processes comes with several challenges, as discussed in the SI and Table S1. Despite these challenges, electrochemical liquid EM data can provide fundamental insight into the nanoscale behavior of metal dendrites, 31,34 electrodeposition, 35 catalysts, 36 polymerization, 37 and solidliquid battery interfaces. 38,39 However, no publications exist using electrochemical liquid EM to study the dissipative self-assembly processes that create active materials. Studying active molecular materials via liquid EM poses its own set of challenges. These materials often have low contrast, are highly dynamic, and are sensitive to the electron beam. Liquid EM of low contrast and beam-sensitive materials is typically achieved by imaging large structures or using extended exposure times to improve signal-to-noise ratios with a minimal electron dose. 30,40 This, however, is insufficient for capturing the intricate details of molecularly active materials, which require both high spatial and temporal resolution.

Here, we study the nanoscale self-assemblies of an electrochemically driven reaction network using liquid EM. The driving force of the chemical network, shown in Figure 1a, is the electrochemical oxidation of the free cysteine thiol precursor (CSH) molecule to its disulfide gelator form (CSSC) using the ferricyanide/ferrocyanide redox couple as a electrochemical catalyst. 14 CSSC molecules then self-assemble into fibers. The assemblies are transient due to the presence of dithiothreitol (DTT) which chemically reduces CSSC back to CSH, effectively disassembling the fibers.⁴¹ We show the deconvolution of imageable beam effects from nonbeam-induced phenomena such as the self-assembly process. We used in situ electrochemistry to show the assembly and disassembly of these structures with nanoscale resolution in two different spatiotemporal regimes. We show spatiotemporal control over the modification of the already formed material and its reaction history dependence. Finally, we computationally verify how the observed history dependence may stem from specific alterations of the rate parameters in the rate equations.

RESULTS AND DISCUSSION

In situ electrochemical liquid EM experiments were performed using a DENSsolutions Stream Holder. 14,42 The Stream houses a top and bottom silicon nitride-coated silicon chip set (Figure 1b). When assembled, the chip set forms an on-chip microfluidic channel. A flow-controlled fluidic pump gives the capability for a controlled flow of sample across the imaging area. 42 Controlled flow was used between electrochemical experiments to refresh any depletion of reagents with a fresh solution. All electrochemical experiments presented were performed under a noflow condition. Patterned on the bottom chip are a platinum counter, pseudoreference, and working electrodes (Figure 1c). A comb-shaped working electrode overlaps with the electrontransparent window. After liquid flows into the nanocell, this overlap allows imaging to take place at the solutionlelectrode interface (Figure 1d). Our experiments use the working electrode as an anode. This provides the driving force for the

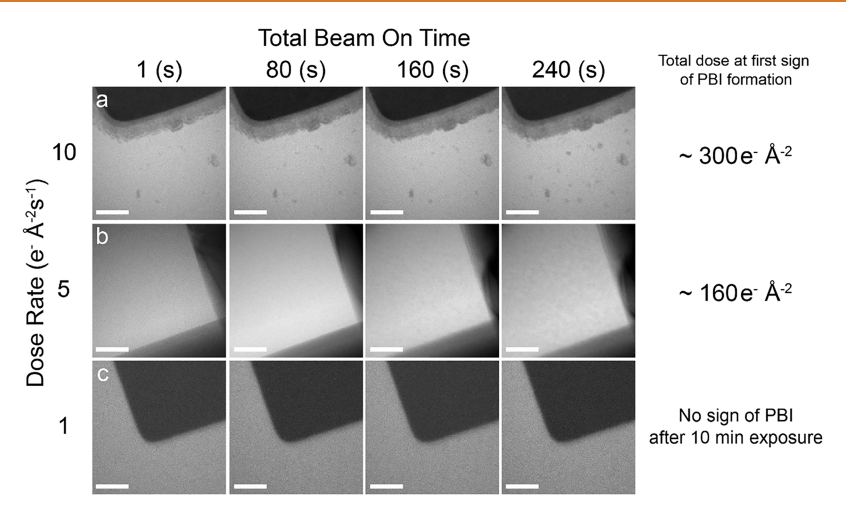


Figure 2. Liquid EM control experiments. Time series panels showing PBI morphology changes with respect to the electron beam dose rate. No electrochemical stimulus or fluid flow was applied during these experiments. All scale bars are $1\,\mu\text{m}$. (a) At a relatively high dose rate of $10\,\text{e}^-\,\text{Å}^{-2}\,\text{s}^{-1}$, cube-like formations result. After approximately $300\,\text{e}^-\,\text{Å}^{-2}$, PBI particles appear and grow. (b) At a medium dose rate of $5\,\text{e}^-\,\text{Å}^{-2}\,\text{s}^{-1}$, a PBI amorphous film is produced throughout the entire viewing area. The first sign of this PBI is after approximately $160\,\text{e}^-\,\text{Å}^{-2}\,\text{e}^-\,\text{Å}^{-2}$ of electron dose has occurred. (c) For the CSH system, an acceptable dose rate of $1\,\text{e}^-\,\text{Å}^{-2}\,\text{s}^{-1}$ was found. At this electron dose, no imageable beam-induced effects could be seen. This dose rate was tested up to a total continuous time of $10\,\text{min}$.

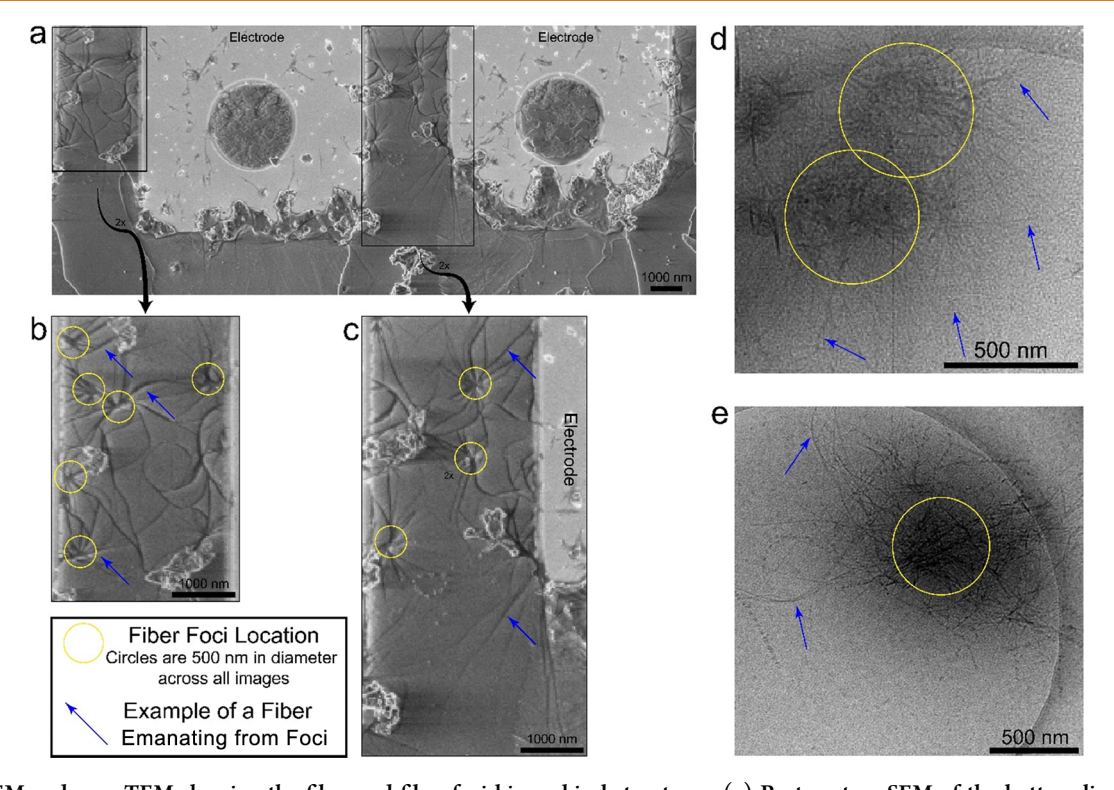


Figure 3. SEM and cryo-TEM showing the fiber and fiber foci hierarchical structures. (a) Postmortem SEM of the bottom liquid cell chip showing multiple fiber and fiber foci near the working electrode. (b,c) Two times magnified crops corresponding to the black rectangle outlined in (a). The yellow circle overlays are centered over some examples of fiber foci. Each circle has a diameter of 500 nm, which is scaled to the image it overlays. The scaled yellow circles help the reader easily compare the SEM and cryo-TEM images (d,e). The blue arrows show a few examples of fibers emanating from the fiber foci. (b) shows three foci closely overlapping one another, two of which have 500 nm yellow circles overlaid. (e) shows another, higher contrast, fiber foci/fiber hierarchical structure. Fiber measurements from these and other postmortem SEM images show diameters of 22.0 ± 1.5 nm. Fiber measurements from cryo-TEM show a fiber diameter of 21.2 ± 2.8 nm.

oxidation of ferrocyanide to ferricyanide and the follow-up oxidation of CSH to CSSC, as shown in the reaction diagram in Figure 1a.

To gain insight into this system's electron beam-sample interactions, a series of control experiments were performed. This is to account for the imageable effects the electron beam

can have on the sample. We classify these effects as primary beam interaction (PBI) products. Conversely, products derived from the electrochemical system are classified as products of interest (POI). As has been discussed previously, electron beams will cause radiolysis, charging, and heating for all liquid samples, and some of these effects are nonimageable.⁴³ To characterize

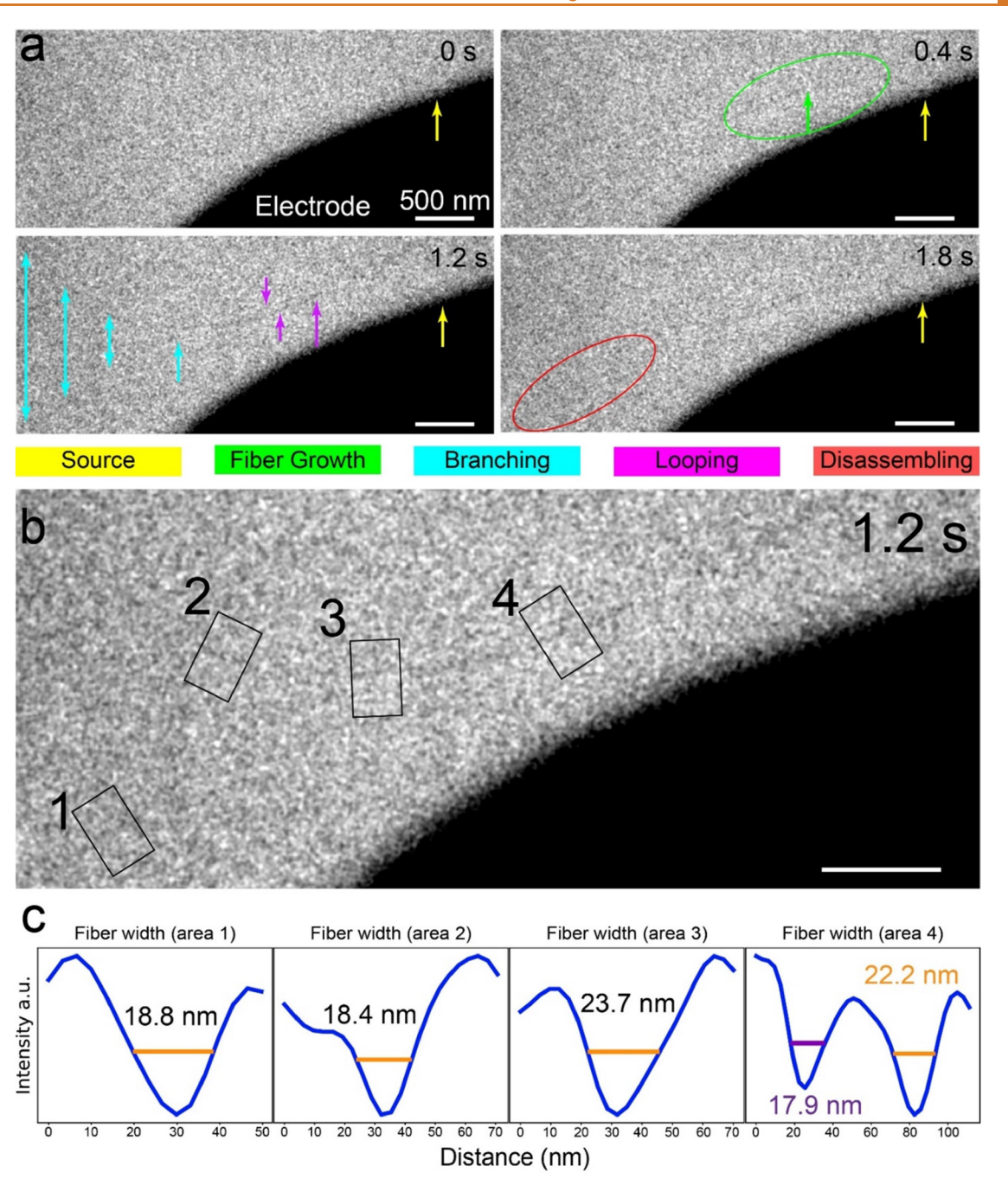


Figure 4. Liquid EM active materials dynamics at short time scales. Liquid EM experiment was performed using a chronoamperometry experiment with no liquid flow at a dose rate of $0.0712 \, {\rm e}^{-} \, {\rm A}^{-2} \, {\rm s}^{-1}$. All times are taken with respect to the beginning of fiber growth. Scale bars are 500 nm. (a) Selected frames showing dynamics of a single fiber. At t=0 s, the yellow arrow is pointing to where the fiber emerges past the electrodelliquid boundary. At t=0.4 s, the green arrow highlights the area the fiber grew between 0 and 0.4 s. At t=1.2 s, the purple arrows show fiber looping where the fiber branches and reconnects. Additionally, the blue arrows point at the branching fibers and the point in which the branch begins. At t=1.8 s, the red oval shows the area where one of the branches disassembles between 1.2 and 1.8 s. (b) Using the frame from t=1.2, fiber widths were measured. Boxes 1-4 denote the area in which the measurement was taken. Measurements are the average of line profiles along the direction of the fiber. (c) Plots of the full width at half-maximum of the fiber width measurements from 3b, the average of which is 19.2 ± 2.4 nm.

these two classes of products (PBI products and POI), we studied their formation using the electron beam and electrochemical stimulus. For example, electron beam dose rates of 10, 5, and 1 e^- Å $^{-2}$ s $^{-1}$ were used with no oxidative potential applied to ensure that any imageable products are PBI. Varying the electron beam dose rate allows the exploration of different kinetic regimes of PBI products. Figure 2a shows at an electron beam dose rate of $10 e^-$ Å $^{-2}$ s $^{-1}$ particles began to form and grow

at approximately 30 s or a total dose of 160 e Å $^{-2}$. These particles exhibited cube-like morphology by both liquid EM and postmortem scanning electron microscopy (SEM) (Figure S1). Importantly, these particles do not disassemble or reorganize after the electron beam is turned off. At 5 e^- Å $^{-2}$ s $^{-1}$, a low contrast discontinuous film formation started at approximately 32 s of exposure or a total dose of 160 e Å $^{-2}$ (Figure 2b). At 1 e^- Å $^{-2}$ s $^{-1}$, no particle or film formation is

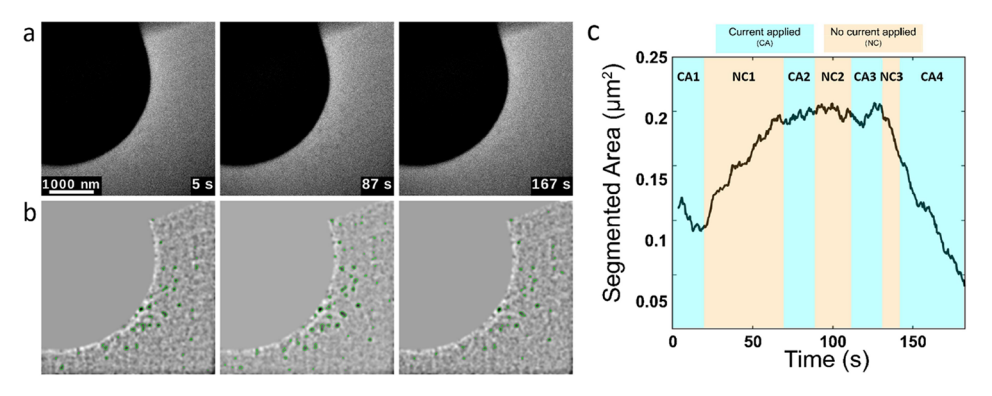


Figure 5. Liquid EM fiber foci formation and disassembly. (a) Selected images showing fiber foci early growth (t = 5 s), max growth (t = 87 s), and disassembly (t = 167 s). These images are made up of 10 (1 s) raw images averaged together. Row a corresponds to the left panel of Movie 1. (b) Bottom row of images is temporally binned to 7 s and flattened using Gaussian filters (details in the SI). Row (b) corresponds to the middle panel of Movie 1. (c) Plot of the total segmented structure area versus time. Also shown are the time periods in which current was applied (teal) and time periods in which no current was applied (tan). The liquid cell was at a no-flow condition during all CA and NC time periods.

observed for up to 10 min (Figure 2c), and consequently, we defined $\leq 1 e^{-} \text{Å}^{-2} \text{s}^{-1}$, and a total dose of 600 e Å⁻² as low dose imaging for these experiments. Ten minutes of exposure was chosen as this time corresponds to the length of our longest electrochemical data set.

Further control experiments were conducted to determine the necessary chemical conditions for forming the POI. This was accomplished by systematically testing reagent combinations and electrochemical stimulus conditions (Table S2). These experiments showed that all reagents required for the growth of the active material in a bulk solution are also required in the electrochemical liquid EM experiment. 14 Postmortem SEM images of the bottom liquid EM cell reveal the formation of nanofiber network morphology (Figures 3 and S2). The SEM images in Figure S3 show that POI is present both far away from and within the direct beam interaction area indicating that these POI networks can grow under the defined low-dose imaging conditions. The SEM images in Figure 3a,b are representative images that show areas of dense deposition at or very near the electrode boundary verified by atomic force microscopy (AFM) (Figure S4). We have termed these dense regions as fiber foci as they appear to connect multiple individual fibers. CryoTEM images confirmed that the system forms a hierarchical structure composed of ~20 nm fibers and localized areas of high material density, the fiber foci (Figure 3d,e). Our data indicate that, absent fiber foci, we see no fiber growth unless the fiber is directly emanating from the working electrode (Figures 3 and S2). The fiber/fiber foci hierarchical structure is also consistent with our previous work on the CSSC hydrogel system. 14,15,44

To capture the dynamics of this hierarchical material, we collected in situ data at multiple magnifications and frame rates. At higher magnifications and shorter frame rates, we can capture single fiber growth and dynamics. At lower magnifications and longer frame rates, we can track the dynamics of the fiber foci. For the lower magnification experiments, the network growth was electrochemically initiated during a period in which the electron beam was turned off. Preforming the active material enables tracking the dynamics over larger length scales.

Active Material Dynamics at Short Time Scales. To perform in situ electrochemical synthesis of the active material, all reagents were flown into the holder while the beam was blanked and then subsequently imaged in a no-flow condition. To study the formation of fibers on an individual level and their short time scale dynamics, we utilized a Gatan Metro in situ

direct detector at a minimum of ten frames per second exposure

Figure 4a shows a time series of fiber growth and dynamics at the electrode surface over a period of 1.8 s. Within this time, the image series appears to show the emergence of the fiber at the electrode boundary, which continues to grow while going through a series of branching and looping events and then shows partial disassembly before completely disappearing. To combat the low signal-to-noise ratio while maintaining temporal resolution, we used a five frame, or 0.5 s, sliding exponential window function along the time axis. A Gaussian blur using a sigma value of 1.5 or 4.65 nm was then applied on the x and yaxis. This produces a smoothed data set along the x and y spatial axis and along the time axis. For this data, the exponential weighting was chosen to allow the reader to better see the fiber and achieve good fiber measurements. We must note here that some of the fiber dynamics could be explained by attachment or detachment from the silicon surface. However, given the directionality of growth, it is reasonable to attribute this to dynamical growth and disassembly of the fiber. Figure 4b shows the areas in which fiber measurements were taken. The full width at half-maximum of the fiber width measurements shows fiber widths between 19.2 ± 2.4 nm (Figure 4c). These widths are consistent with cryo-TEM measurements of the electrochemically stimulated fibers and the postmortem SEM (Figure 3).

Previous work has shown that the decoupling of beam interaction from the electrochemical formation of the product can be accomplished via a comparison of a beam-always-on versus a beam on-off-on scheme.45 If the kinetics and dynamics are the same between these two experiments, then there are no imageable beam effects on the formation/ deformation of the POI. However, active materials are highly stochastic, making repeatable dynamics measurements extremely challenging.⁴⁶ Consequently, we were unable to perform a beam on-off-on scheme; however, we performed the experiments at $0.5-0.1 e^{-} \text{Å}^{-2} \text{s}^{-1}$. This dose is well below the low dose conditions established above, and consequently, we classify these fibers as POI. Importantly, growth, branching, and disassembly are all behaviors consistent with active materials dynamics and is significantly different behavior to the PBI observed in Figure 2a,b. 6,14,15,4

Fiber Foci Formation and Dissolution. Four chronoamperometry experiments were performed while imaging at 0.091 e^{-} Å⁻² s⁻¹, which enables us to analyze how the system responds

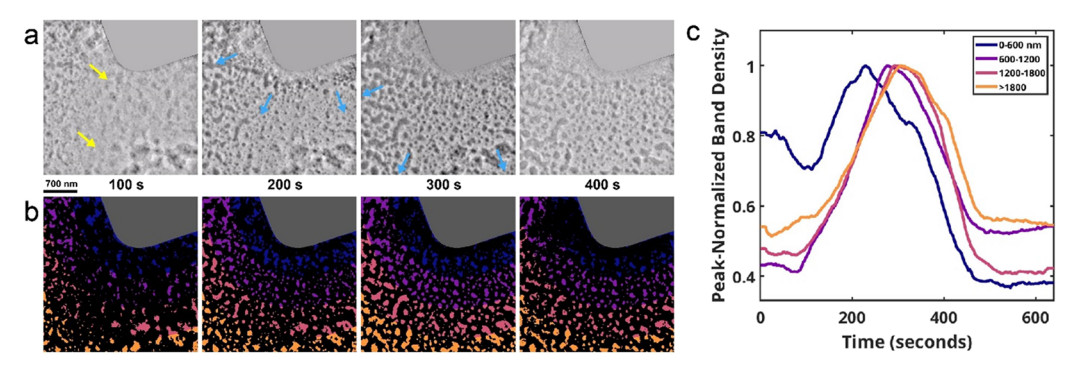


Figure 6. Liquid EM of fiber foci modification. Area of segmented particles versus time. (a) Snapshots of Movie 3 left panel at times of interest. Yellow arrows at time 100 s show the path through which front 1 travels. Blue arrows at times of 200 and 300 s show the path front 2 travels. (b) Segmented particles corresponding to the images in (a) and the middle panel of Movie 3. Here, the imaging area is divided into four areas, with boundaries defined by distance from the electrode (details in SI). (c) Graph showing the normalized change in segmented particle area versus time for each region. The divided regions are represented by the blue (closest to the electrode), purple, red, and yellow (farthest from the electrode) colors. The graph shows an increase and then a decrease in particle area in all regions. The time sequence in which the divided regions reach a global maximum shows a correlation with distance from the working electrode (Movie 3, right panel). Electrochemical stimulus was applied in the form of a chronopotentiometry experiment. The liquid cell was in a no-flow state during the experiment.

when the current is turned on and off (Movie 1). Figure 5a shows temporally averaged TEM images taken from Movie 1 (left panel) corresponding to the beginning of foci growth (5 s), peak of foci growth (87 s), and foci disassembly (167 s). To quantify our observations, we measured the total density of structures in each frame of the electrochemical liquid EM video using segmentation analysis (Figure 5b). Details of this analysis can be found in the Supporting Information (Figures S5-S7). The segmented structures are outlined in green, and the total area is calculated for every frame and plotted against time (Figure 5c). This area versus time graph shows an overall trend of growth in the structure area and subsequent shrinking of the structure area, which is consistent with the behavior of an active material. Figure 5c also shows the time periods for the four chronoamperometry (CA) experiments performed (CA1-4) and periods of no applied potential (NC1-3). The overall growth and shrinking of the fiber foci appears to loosely correlate with application and removal of electrochemical stimulus. CA1 shows an initial drop in structure area, which then increases after a delay of approximately 10 s. The structures appear to continue growing during NC1, indicating that there is a kinetic delay of material. We also see a subtle increase in structure growth during CA2-3 and decreases during NC2-3. Interestingly, the final application of stimulus (CA4) does not result in further assembly but instead results in a decrease in structure area. This data differs from bulk observations that show a strong correlation between fiber growth and applied potential. 14,15

Examination of the electrochemical data suggests that two things may be responsible for this disparity between the bulk experiment versus liquid EM experiment. The first is the peak current delivered in each CA experiment. Electrochemical data shows a decrease in current with each CA experiment. This suggests a decrease in the initial concentration of the redoxactive species with each application of potential (Figure S8). This decreasing initial concentration may account for the decreasing effect that each successive CA experiment has on the particle growth. Second is the change in the diffusion coefficient of the redoxactive species. The diffusion coefficient of a thin film can be found by constructing a current (i) versus $t^{-1/2}$ plot or Cottrell plot, the slope of which is $\frac{nFA\sqrt{D}C_0}{\sqrt{\pi}}$ where n=1 number of electrons transferred per molecule, F=1 Faraday's constant, A=1

WE area, D = diffusion coefficient, and C_0 is the initial concentration of the redox active species. The slopes of the first three CA experiments show little change; however, a six-fold decrease in the slope occurs between the third and fourth applications of potential (Figure S9). This decrease in the current response rate may be due to an increase in viscosity. The combination of the low initial concentration and decrease in the diffusion rate of the redox-active species may have allowed DTT-driven disassembly to dominate. This would lead to the decrease in particle area seen during the fourth application of the potential.

Fiber Foci Modification. We electrochemically preformed the active material to study its dynamics in response to further electrochemical stimulus. Current was applied to the existing structures; at the same time, the electron beam was turned on (t = 0 s) and held constant for the duration of the experiment (Movie 2). For the first 100 s, the fiber foci appear relatively stable, with very little change occurring. At 100 s, a self-assembly "growth front" (front 1, yellow arrows) propagates from left to right in a wave-like manner across the viewing window and causes the structures to grow and increase in contrast. At 200 s, another growth front (front 2, blue arrows) is formed as front 1 reaches the electrode boundary. Front 2 propagates outward from the electrode in all directions. From 400 to 600 s, the structures begin to break down, shrink, and become lower contrast across all regions of the viewing window.

To quantify the observed wave-like propagation of these selfassembly fronts, regional segmentation analysis was performed (Movie 3 and Figure 6). Full details of this analysis can be found in the Supporting Information (Figure S10). Figure 6a shows the flattened TEM images, and Figure 6b shows the corresponding structure segmentation maps. To resolve the spatiotemporal behavior of the fronts, regional density analysis was performed on the segmentation maps. To resolve front 2, the segmentation maps were split into four different 600 nm thick regions based on distance from the electrode. For each frame, the object density in each region was calculated and then normalized to the respective maximum density. This enabled a direct comparison of the times at which the structures reached the maximum size in each region. Figure 6c shows that maximum structural density occurs sequentially based on the distance from the electrode, which confirms the qualitative observation of the outward-moving

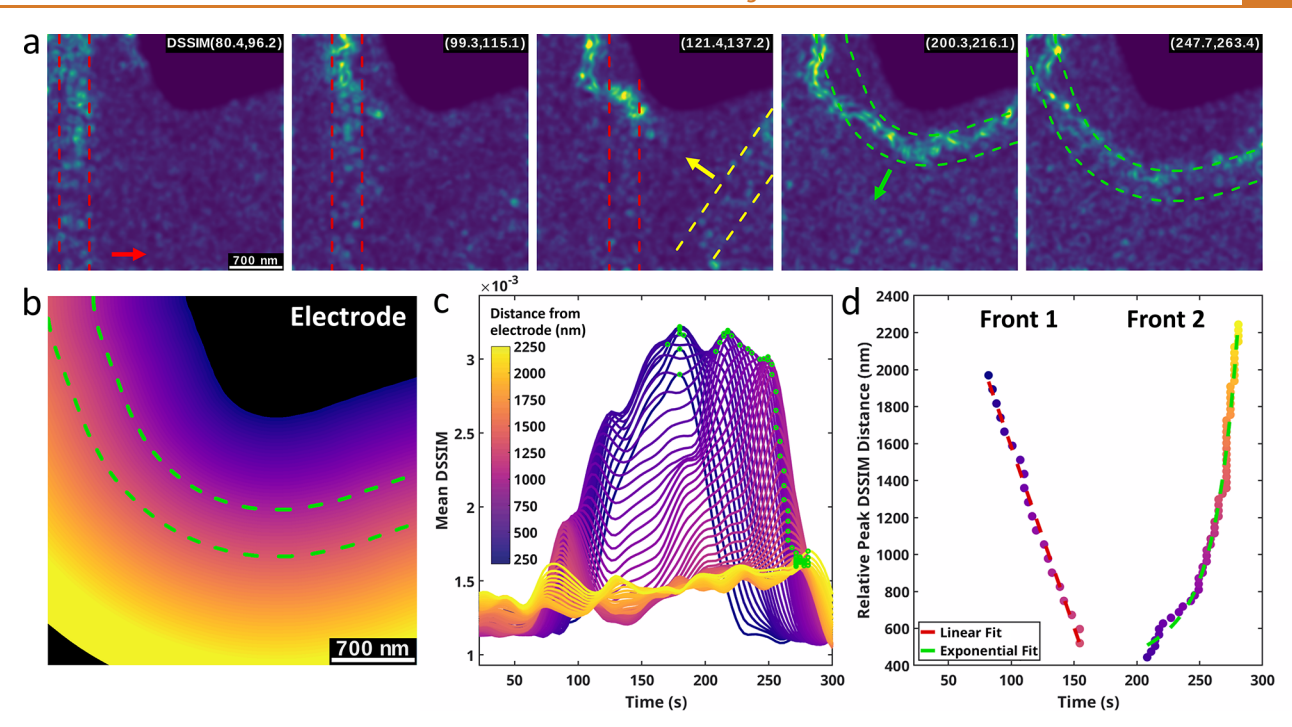


Figure 7. Visualization and quantification of fiber foci dynamics. (a) Dissimilarity images from DSSIM analysis. Bright pixel values correspond to regions of high dissimilarity between frames. Top time labels correspond to the times (seconds) of the two Liquid EM images used to calculate the DSSIM image. (b) Image was divided into 70 overlapping regions, each 400 nm thick, based on distance from the electrode. The dashed line shows the size of 1 region. The color gradient shows the distance from the electrode for each of the 70 regions, with purple being closest to the electrode and yellow the furthest. (c) Mean DSSIM signal of each region versus time. The green dots mark the maximum dissimilarity for each region. (d) Progression of the regional DSSIM maximums for both front 1 (Figure S12) and front 2. Front 1 shows a linear velocity while front 2 is accelerating.

front 2. Interestingly, there appears to be a large time delay between the 0-600 region and subsequent regions, implying that front 2 may be accelerating and moving more quickly through regions that are further from the electrode. Regional analysis was also applied to resolve front 1 in which the regions were defined vertically based on distance from the left edge of the image (Figure S11). Again, the analysis clearly resolves the self-assembly growth front as it moves across each region.

To better visualize and quantify the structural change occurring in the liquid cell, structural dissimilarity (DSSIM) analysis was applied to the electrochemical liquid EM video (Figure 7 and Movie 4). 14,53,54 DSSIM analysis is a video processing algorithm that spatially and temporally quantifies structural changes occurring in a video. The algorithm compares the pixel intensity values between local regions of temporally offset images of the video to highlight and measure structural changes based on differences in mean, variance, and cross-correlation. DSSIM analysis was applied to the processed frames with a local neighborhood of 186 nm (61 pixels), 15.8 s offset (5 frames), and [1 1 1] coefficients (details in the SI). DSSIM analysis clearly highlights the structural change resulting from fronts 1 and 2.

To quantify the characteristics of fronts 1 and 2, regional analysis was performed on the DSSIM data (Figures 7 and S12). Like Figure 6b, the image was divided into several 400 nm thick regions based on distance from the electrode. In this case, 36 overlapping vertical regions (Figure S12a) and 70 overlapping distance regions (Figure 7b) were defined, which provided a higher spatial resolution while maintaining an adequate sample size within each region. To resolve the magnitude of the structural change spatially and temporally, the mean DSSIM

value was calculated for each region in every frame (Figure 7c). Figures 7c and S13 shows structural dynamics are greatest in the regions <1000 nm from the electrode and then substantially decrease in the regions >1000 nm from the electrode, consistent with previous confocal laser scanning microscopy data on this chemical system.¹⁴ This observation suggests that there is a spatial dependence with respect to the electrode on the interaction between the electrochemically generated oxidant and the CSH reductant. Next, the velocities of front 1 and front 2 were quantified by finding the time at which the maximum DSSIM value occurs for each region (Figure 7c, green dots, and Figure S12b). This represents the time at which the structural change is at a maximum within each region. Plotting the maximum time against the average region distance results in a distance—time graph. Fitting front 1 with a line shows the front is moving at constant velocity. Fitting front 2 with an exponential fit shows the front is positively accelerating and confirms the observation made from the segmentation analysis.

Figure S14a,b and Movie S1 show the DSSIM signal within the spatial context of the surrounding liquid EM cell. A correlation can be seen between front 1 and the shape of the adjacent working electrode "tooth". In addition, DSSIM analysis resolves another front moving from the right to left across the viewing window, which appears at a similar time to front 1 (Figure 7a, 3rd panel Figure S14c). This agrees with a subtle increase in segmented particle area on the right side of the viewing area that is not correlated with either front 1 or 2 (Figure S11c, black arrow). An additional chronopotentiometry experiment is shown in Movie S2 which shows the presence of frontal dynamics associated with the electrochemical stimulus. To

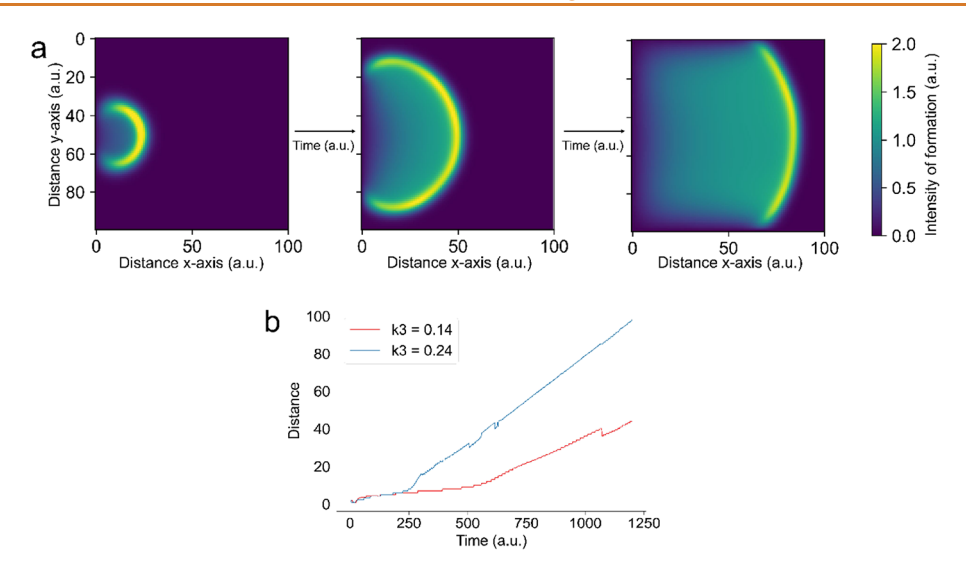


Figure 8. Simulations and schematic representation of active material dynamics. (a) Three snapshots (at three times) of the "wave" of self-assembled material were obtained from simulations. A region at the center of the left boundary mimics the electrode by injecting fuel for a finite time. A "solitary" wave appears as a result of fueling the chemical reactions and self-assembly, which expands laterally as it travels to the far side. The features of these simulations agree with experimental observations. (b) Speed of wave increases with the magnitude of the self-assembly constant k_3 .

better interpret the liquid TEM data, we turned to chemical kinetic simulations.

Simulations of the Active Material Dynamics. To better understand the relationship between the underlying chemical kinetics and the production of the material waves, we constructed a minimal model for the chemical reactions, self-assembly, and diffusion (see Methods). We simulated the concentrations of active u and inactive chemical species v over time with the reaction—diffusion equations.

$$\begin{split} \frac{\partial u}{\partial t} &= D_u \nabla^2 u - k_1 u f_1 + k_2 v f_2 + k_3 u^2 \\ \frac{\partial v}{\partial t} &= D_v \nabla^2 v - k_1 u f_1 - k_2 v f_2 - k_3 u^2 \\ \frac{\partial f_1}{\partial t} &= D f_1 \nabla^2 f_1 - k_1 u f_1 \\ \frac{\partial f_2}{\partial t} &= D f_2 \nabla^2 f_2 - k_2 v f_2 + r \end{split}$$

with rate constants k_1 , k_2 and k_3 for production, depletion, and self-assembly, respectively. The chemical "fuels", f_1 and f_2 , drive the kinetics of the activation/deactivation reactions and assembly. The reaction-diffusion equations were solved with the finite-difference method on a 100 × 100 grid. As initial conditions, uniformly distributed random values of ν and f_1 in [0,2] were generated throughout the reaction volume. The rate and diffusion constants were $(k_1, k_2, k_3) = (0.22, 1.7, 0.23)$ and $(D_{\nu}, D_{\nu}, D_{f_1}, D_{f_2}) = (1.5, 0.1, 0.1, 1.8)$. To mimic the experiments, fuel f_2 was injected at a rate r for a short period of time (25 time steps; see methods for details). These simulation parameters were chosen by examining the effect of each from a sweep of their values over a range in which the simulations were numerically stable. Several dynamical behaviors were observed that are robust over the parameter values considered. The simulations show wave-like dynamics of the assembled material (Figure 8a). Deactivation (and disassembly) dominates in the spatial regions behind the wavefront, causing a solitary wave and

corroborating the experimental observations. The rate constants for activation/deactivation set characteristic time scales for the initiation of the dynamic pattern. The wavefront propagates when fuel is injected at a constant rate for a time longer than the characteristic times, $1/k_1$ or $1/k_3$).

The most notable feature of the driven reaction-diffusion model is that it provides a plausible explanation for the observed acceleration in the speed of the material wavefront, as shown in Figure 7d. Simulations show that increasing the rate of selfassembly k_3 accelerates the wavefront (Figure 8b). To understand this effect, the parameter k_3 was varied between the values 0.14 and 0.24 in the steps of 0.1 (the curves for two representative values, 0.14 and 0.24, are shown in Figures 8b and S15). In the numerical analysis, the wave speed is defined as the distance traveled by the peak per unit time. The dependence of the wave speed on the self-assembly rate constant supports the experimental observation that front 2 forms in an area with higher contrast (Figure 6a), which we interpret as an area with higher material density and appears to accelerate. This isolation of the key mechanistic step is important because it shows that local formation of the active material network can result in a local increase in the rate of self-assembly, effectively autocatalyzing the formation of material structure.

CONCLUSIONS

In this study, we employed a combination of liquid electron microscopy, electrochemical analysis, quantitative video analysis, and kinetic simulations to explore an electrochemically fueled active soft material system. Through control experiments, we distinguished the influence of the electron beam from the intrinsic dynamics of the electrochemical active material. We captured single fiber dynamics at subsecond temporal resolution and larger transitory fiber foci structures with nanoscale resolution. Our findings reveal that the dynamics of these materials is influenced by both the electrical input and the local structure. Furthermore, we demonstrated that the active material can be dynamically manipulated to form multiple growth fronts influenced by electrodes at various spatial locations. Additionally, by combining liquid electron micros-

copy data with kinetic simulations, we discovered that the formation of an active material can create a local environment that accelerates the self-assembly rate, exhibiting an autocatalytic behavior. This underscores the importance of liquid electron microscopy in active material research, providing essential insights into the relationship between chemical kinetics and material dynamics.

METHODS

Materials. All reagents were purchased at the indicated quality and used without further purification. Methanol (MeOH) (ACS grade) potassium ferrocyanide trihydrate (reagent grade), sodium chloride (NaCl) (ACS grade), dibasic sodium phosphate heptahydrate (Na₂HPO₄·7H₂O) (ACS grade), sodium hydroxide (NaOH) (ACS grade), and DTT (98%) were purchased from Fisher Chemical. (R)-N-(1-Amino-3-mercapto-1-oxopropan-2-yl)benzamide (CSH) was synthesized based on the literature procedure. 41

Preparation of CSH Aqueous Solution for Electrochemical Liquid EM. The standard solution consists of the following reagents at their final concentrations: 2.5 lmMl CSH, 20 lmMl DTT, 100 lmMl $K_4[\text{Fe}(\text{II})(\text{CN})_6]$, 100 lmMl KCl, and 100 lmMl phosphate buffer at pH 7. CSH was first dissolved in warm MeOH to a concentration of 100 lmMl. In a separate vial, all other reagents were dissolved in the appropriate amount of phosphate buffer. Then, the CSH solution was added.

Electrochemical Liquid-Phase Electron Microscopy. Sample Preparation. Electrochemical liquid EM samples were prepared within 6 h prior to the experiment in a capped vial. Immediately prior to the electrochemical liquid EM experiment, the vial was uncapped, and solution was dispensed into a 1 mL centrifuge tube using a plastic syringe equipped with a 0.20 μ m syringe filter.

Electrochemical Liquid-Phase Electron Microscopy Holder Preparation. Electrochemical Liquid EM experiments were conducted using a DENSsolutions Stream liquid-phase electron microscopy system. All system fluidic lines were cleaned using a 95:5 water to methanol mixture and flowed at 1.7 μL min⁻¹ overnight. All holder fluidic components, other than the micro-electromechanical systems (MEMS) chip set, were submerged in a 50 mL beaker filled with a 95:5 water to methanol solution. The beaker was then placed in a heated (50 °C) sonication bath for 10 min. This was completed twice and once more in pure methanol. Components were dried on lint-free microscopy paper and reassembled. A steal "dummy" chip was installed in the Stream holder tip and then plasma cleaned. It was then inserted into a benchtop high vacuum leak tester to a pressure of 8.9×10^{-6} hPa to ensure reassembly was vacuum tight and then removed from the tester. A top and bottom DENSsolutions biasing chip set in perpendicular configuration was plasma cleaned for 5 min using a 50:50 Ar to O₂ ratio. The MEMS chips were then immediately installed into the holder and rechecked for leaks. After the holder was inserted into the TEM, a Ivium Technologies CompactStat.h potentiostat was connected to the holder using connectors provided by DENSsolutions. CompactStat.h was used in USB-powered mode. All electrochemical experiments were performed during a no-flow state. A no-flow state is when no pressure or vacuum is applied to the liquid channel, and the flow meter shows no flow.

Imaging and Dosage Calculation. Imaging was accomplished using a JEOL 2800F microscope operating at 200 keV in the TEM mode. This TEM was equipped with a Gatan Metro in situ Direct Detection camera and a Gatan OneView in situ CMOS. Both imaging platforms used DigitalMicrograph software for their operation. When using Metro IS, the electron dose rate is calculated by the DigitalMicrograph software during exposure. To get an accurate electron dose rate, the Metro IS was exposed to an electron beam unimpeded by a sample under the same beam conditions used during imaging. When using the OneView IS, the electron dose rate was calculated using the average intensity of an electron beam unimpeded by a sample under the same beam conditions used during imaging. The average intensity value was converted using an empirical conversion factor produced from a built-in faraday cup.

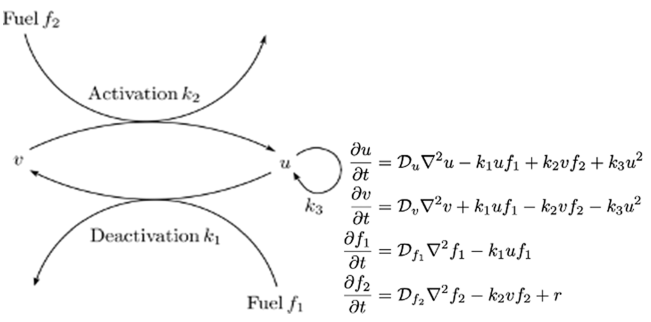
Cryogenic-Transmission Electron Microscopy (Cryo-TEM).

Cryo-TEM samples were prepared electrochemically using a CompactStat potentiostat (Ivium Technologies), standard calomel electrode (CH Instruments), and glassy carbon working and counter electrodes (SPI Instruments). Cryo-TEM samples were prepared using an Automatic Plunge Freezer ME GP2 (Leica Microsystems) and Quantafoil R2/2 TEM grids (Electron Microscopy Sciences). The grids were plasma cleaned using a 50/50 Ar/O $_2$ gas mixture for 10 s. Seven microliters of the formed gel sample solution was obtained from the surface of the working electrode and quickly deposited on the grid in a controlled environment of 98% relative humidity at 20 °C. Immediately after deposition, the grid was blotted for 3 s and plunged into liquid propane at $-180\,^{\circ}$ C. Grids were loaded into a Gatan Cryo-TEM holder and imaged using a JEM-2100F operating at 200 keV in TEM mode. Images were recorded using DigitalMicrograph (Gatan) software with a Gatan OneView CMOS camera at 4k \times 4k resolution.

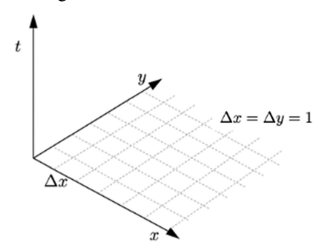
Scanning Electron Microscopy. Imaging was performed directly on the DENSsolutions Stream bottom biasing MEMS chip. All chips were imaged within 1 day of the electrochemical liquid EM experiment that produced them. All SEM imaging was performed on as-is samples, with no metallic coating applied. Samples were imaged with an FEI Magellan 400 XRH system. Images were captured using both an Everhart-Thornley Detector and a Through-The-Lens Detector in immersion mode. All images were taken at an accelerating voltage ranging from 1 to 5 keV and currents of no greater than 50 pA.

Atomic Force Microscopy. Imaging was performed directly on the DENSsolutions Stream bottom biasing MEMS chip. All AFM imaging was performed on as-is samples with no metallic coating applied. Samples were imaged with an Anton Parr Tosca 400 AFM instrument using contact tapping mode.

Numerical Simulations of a Reaction-Diffusion Model.



To understand the observation of a solitary wave of self-assembled material, we constructed a reaction—diffusion model for the key features of the chemical reaction network. The driven reaction—diffusion equations are given next to the reaction schematic above.



As mentioned in the main text, u and v are the concentrations of active and inactive species. Their kinetics are determined by k_1 , k_2 , and k_3 , the production, depletion, and assembly rate constants, respectively. The deactivation and activation fuels have concentrations f_1 and f_2 , respectively. Diffusion coefficients for u, v, f_1 , and f_2 are D_w D_{f^1} , D_{f^2} and D_{f^2} , respectively. The set of parameters was $(k_1, k_2, k_3) = (0.22, 1.7, 0.23)$ and $(D_w$ D_{f^1} , D_{f^2} D_{f^2} is injected for 25 time steps of the 500–1000 step simulations. The stability of the simulations constrains sweeps of the parameter space. To find numerical solutions of the reaction diffusion equations in two dimensions, the finite-difference method was used. This algorithm approximates derivatives by discretizing both space and time, which affects stability and solution

ACS Nano www.acsnano.org Article

accuracy. Initially, a set of small values are sampled from a uniform distribution in [0,2] for the deactivated material and the deactivating "fuel" on the spatial grid. These values are chosen to be large enough to allow for disassembly of u at a rate but small enough to observe the wavefront. For the step size, we use $\Delta t = 0.1$, and the grid has been discretized in cells of size $\Delta x = \Delta y = 1$ in all simulations. The activation fuel f_2 is supplied from a local region along one of the boundaries, which generates activated material u.

At the onset of the simulations, the concentration of the active species *u* is set to zero. For the geometric simplicity of the injection slab, fuel f_2 was injected from a portion of the left boundary of the grid at each step of the simulations. This spatial location of the fuel injection, the "injection slab", mimics the experimental setup in which the fuel is injected into the reaction cell by the electrodes. In simulations, the injection rate is a constant term of 1.2 in the partial differential equations that is set to zero after 25-time steps. This portion is the central region of the left boundary of length 5 (between grid points (0, (45) and (0,55). A well-defined wavefront is observed that expands and has a clear peak in the concentration of u on the simulation grid. In the presence of f_2 , the reactive species u self-assemble and create a localized region of high concentration of u. As shown in Figure 7 of the main text, the concentration of the active species *u* forms a wave that spreads out over time to the other side of the grid. As the wave moves away from the injection point, the distance between the maximum concentration of assembled material and the far boundary decreases linearly with time.

In the simulations, the parameters k_3 and D_u were both found to control the wave speed, providing a plausible explanation for the behavior in Figure 6d. Given that front 2 forms in an area with higher contrast (Figure 5a), which can be interpreted as an area with higher gel density, it is unlikely that the increase in wave speed is related to a decrease in D_u ; this parameter would be smaller in regions of high fiber density, which would slow the evolution of front 2. Consequently, the wave speed increase is attributed to an increase in parameter k_3 , the self-assembly rate constant.

ASSOCIATED CONTENT

Supporting Information

The Supporting Information is available free of charge at https://pubs.acs.org/doi/10.1021/acsnano.4c01524.

Movie 1: Liquid EM of fiber foci growth and disassembly (MP4)

Movie 2: Liquid EM of electrochemically driven fiber foci modification (MP4)

Movie 3: Liquid EM of fiber foci modification (MP4)

Movie 4: DSSIM visualization and quantification of fiber foci dynamics (MP4)

Movie S1: DSSIM analysis in spatial context (MP4)

Movie S2: Liquid EM of frontal dynamics (MP4)

Discussion of challenges associated with the imaging of active materials by liquid EM, table describing details of the liquid EM experiments, details of the image processing and analysis, postmortem SEM and AFM images of liquid EM chips, details on electrochemical analysis of the liquid EM experiments, and a figure on the numerical simulations of the waves (PDF)

AUTHOR INFORMATION

Corresponding Author

Joseph P. Patterson — Department of Chemistry, Center for Complex and Active Materials, and Department of Materials Science and Engineering, University of California Irvine, Irvine, California 92697, United States; ⊚ orcid.org/0000-0002-1975-1854; Email: patters3@uci.edu

Authors

Wyeth Gibson − Department of Chemistry and Center for Complex and Active Materials, University of California Irvine, Irvine, California 92697, United States; ocid.org/0000-0001-5652-1006

Justin T. Mulvey — Center for Complex and Active Materials and Department of Materials Science and Engineering, University of California Irvine, Irvine, California 92697, United States; Occid.org/0000-0002-0296-8598

Swetamber Das — Department of Chemistry, University of Massachusetts Boston, Boston, Massachusetts 02125, United States

Serxho Selmani — Department of Chemistry and Center for Complex and Active Materials, University of California Irvine, Irvine, California 92697, United States

Jovany G. Merham — Department of Chemistry, University of California Irvine, Irvine, California 92697, United States;
occid.org/0000-0003-3151-1877

Alexander M. Rakowski — Department of Chemistry, University of California Irvine, Irvine, California 92697, United States

Eric Schwartz – Department of Chemistry, University of California Irvine, Irvine, California 92697, United States

Allon I. Hochbaum — Department of Chemistry, Center for Complex and Active Materials, Department of Materials Science and Engineering, Department of Molecular Biology and Biochemistry, and Department of Chemical and Biomolecular Engineering, University of California Irvine, Irvine, California 92697, United States; orcid.org/0000-0002-5377-8065

Zhibin Guan — Department of Chemistry, Center for Complex and Active Materials, Department of Materials Science and Engineering, Department of Chemical and Biomolecular Engineering, and Department of Biomedical Engineering, University of California Irvine, Irvine, California 92697, United States; orcid.org/0000-0003-1370-1511

Complete contact information is available at: https://pubs.acs.org/10.1021/acsnano.4c01524

Notes

The authors declare no competing financial interest.

ACKNOWLEDGMENTS

This research was primarily supported by the National Science Foundation Materials Research Science and Engineering Center program through the UC Irvine Center for Complex and Active Materials (DMR-2011967). This material is based upon work supported by the National Science Foundation under Grant No. 2124510 (J.G.), 2231469 (J.G.), and CHE-1904939 (Z.G.), and the U.S. Department of Energy, Office of Science, Basic Energy Sciences (DE-FG02-04ER46162; Z.G.) The authors acknowledge the use of facilities and instrumentation at the UC Irvine Materials Research Institute (IMRI) supported in part by the National Science Foundation Materials Research Science and Engineering Center program through the UC Irvine Center for Complex and Active Materials (DMR-2011967).

REFERENCES

(1) Das, K.; Gabrielli, L.; Prins, L. J. Chemically Fueled Self-Assembly in Biology and Chemistry. *Angew. Chem., Int. Ed.* **2021**, *60*, 20120.

- (2) Needleman, D.; Dogic, Z. Active matter at the interface between materials science and cell biology. *Nature Reviews Materials* **2017**, 2 (9), 17048
- (3) Brouhard, G. J.; Rice, L. M. Microtubule dynamics: an interplay of biochemistry and mechanics. *Nat. Rev. Mol. Cell Biol.* **2018**, *19* (7), 451–463.
- (4) Howard, J.; Hyman, A. A. Growth, fluctuation and switching at microtubule plus ends. *Nat. Rev. Mol. Cell Biol.* **2009**, *10* (8), 569–574.
- (5) Aprahamian, I.; Goldup, S. M. Non-equilibrium Steady States in Catalysis, Molecular Motors, and Supramolecular Materials: Why Networks and Language Matter. *J. Am. Chem. Soc.* **2023**, *145* (26), 14169–14183.
- (6) Boekhoven, J.; Hendriksen, W. E.; Koper, G. J. M.; Eelkema, R.; van Esch, J. H. Transient assembly of active materials fueled by a chemical reaction. *Science* **2015**, 349 (6252), 1075–1079.
- (7) Rieß, B.; Grötsch, R. K.; Boekhoven, J. The Design of Dissipative Molecular Assemblies Driven by Chemical Reaction Cycles. *Chem.* **2020**, *6* (3), 552–578.
- (8) Mattia, E.; Otto, S. Supramolecular systems chemistry. *Nat. Nanotechnol.* **2015**, *10* (2), 111–119.
- (9) De Jong, J. J. D.; Hania, P. R.; PugLys, A.; Lucas, L. N.; De Loos, M.; Kellogg, R. M.; Feringa, B. L.; Duppen, K.; Van Esch, J. H. Light-Driven Dynamic Pattern Formation. *Angew. Chem., Int. Ed.* **2005**, 44 (16), 2373–2376.
- (10) Ikegami, T.; Kageyama, Y.; Obara, K.; Takeda, S. Dissipative and Autonomous Square-Wave Self-Oscillation of a Macroscopic Hybrid Self-Assembly under Continuous Light Irradiation. *Angew. Chem., Int. Ed.* **2016**, *55* (29), 8239–8243.
- (11) Klajn, R.; Wesson, P. J.; Bishop, K. J. M.; Grzybowski, B. A. Writing Self-Erasing Images using Metastable Nanoparticle "Inks. *Angew. Chem., Int. Ed.* **2009**, 48 (38), 7035–7039.
- (12) Ross, T. D.; Lee, H. J.; Qu, Z.; Banks, R. A.; Phillips, R.; Thomson, M. Controlling organization and forces in active matter through optically defined boundaries. *Nature* **2019**, *572* (7768), 224–229
- (13) Klajn, R.; Bishop, K. J. M.; Grzybowski, B. A. Light-controlled self-assembly of reversible and irreversible nanoparticle suprastructures. *Proc. Natl. Acad. Sci. U. S. A.* **2007**, *104* (25), 10305–10309.
- (14) Selmani, S.; Schwartz, E.; Mulvey, J. T.; Wei, H.; Grosvirt-Dramen, A.; Gibson, W.; Hochbaum, A. I.; Patterson, J. P.; Ragan, R.; Guan, Z. Electrically Fueled Active Supramolecular Materials. *J. Am. Chem. Soc.* **2022**, *144* (17), 7844–7851.
- (15) Barpuzary, D.; Hurst, P. J.; Patterson, J. P.; Guan, Z. Waste-Free Fully Electrically Fueled Dissipative Self-Assembly System. *J. Am. Chem. Soc.* **2023**, *145* (6), 3727–3735.
- (16) Ragazzon, G.; Malferrari, M.; Arduini, A.; Secchi, A.; Rapino, S.; Silvi, S.; Credi, A. Autonomous Non-Equilibrium Self-Assembly and Molecular Movements Powered by Electrical Energy**. *Angew. Chem., Int. Ed.* 2023, 62 (5), No. 214265.
- (17) Dominguez, R.; Holmes, K. C. Actin Structure and Function. *Annual Review of Biophysics* **2011**, 40 (1), 169–186.
- (18) Merindol, R.; Walther, A. Materials learning from life: concepts for active, adaptive and autonomous molecular systems. *Chem. Soc. Rev.* **2017**, *46* (18), 5588–5619.
- (19) Marolf, D. M.; Jones, M. R. Measurement Challenges in Dynamic and Nonequilibrium Nanoscale Systems. *Anal. Chem.* **2019**, *91* (21), 13324–13336.
- (20) Sebastian, Nicholas; Bohner, G.; Gustafsson, N.; Boutant, E.; Surrey, T. EB1 Accelerates Two Conformational Transitions Important for Microtubule Maturation and Dynamics. *Curr. Biol.* **2014**, *24* (4), 372–384.
- (21) Gell, C.; Bormuth, V.; Brouhard, G. J.; Cohen, D. N.; Diez, S.; Friel, C. T.; Helenius, J.; Nitzsche, B.; Petzold, H.; Ribbe, J.; et al. Chapter 13 Microtubule Dynamics Reconstituted In Vitro and Imaged by Single-Molecule Fluorescence Microscopy. In *Methods in Cell Biology*, Wilson, L.; Correia, J. J. Eds.; Vol. 95; Academic Press, 2010; pp 221–245.

- (22) (acccessed 4/17/2023). Manka, Szymon W.; Moores, Carolyn A. Microtubule structure by cryo-EM: snapshots of dynamic instability. *Essays in Biochemistry* **2018**, *62* (6), 737–751.
- (23) Galbraith, C. G.; Galbraith, J. A. Super-resolution microscopy at a glance. *Journal of Cell Science* **2011**, 124 (10), 1607–1611.
- (24) Schermelleh, L.; Ferrand, A.; Huser, T.; Eggeling, C.; Sauer, M.; Biehlmaier, O.; Drummen, G. P. C. Super-resolution microscopy demystified. *Nat. Cell Biol.* **2019**, *21* (1), 72–84.
- (25) Prakash, K.; Diederich, B.; Heintzmann, R.; Schermelleh, L. Super-resolution microscopy: a brief history and new avenues. *Philosophical Transactions of the Royal Society A: Mathematical, Physical and Engineering Sciences* **2022**, 380(2220) DOI: 10.1098/rsta.2021.0110.
- (26) Bon, P.; Cognet, L. On Some Current Challenges in High-Resolution Optical Bioimaging. *ACS Photonics* **2022**, 9 (8), 2538–2546
- (27) Egerton, R. F.; Watanabe, M. Spatial resolution in transmission electron microscopy. *Micron* **2022**, *160*, No. 103304.
- (28) Yesibolati, M. N.; Laganá, S.; Kadkhodazadeh, S.; Mikkelsen, E. K.; Sun, H.; Kasama, T.; Hansen, O.; Zaluzec, N. J.; Mølhave, K. Electron inelastic mean free path in water. *Nanoscale* **2020**, DOI: 10.1039/d0nr04352d.
- (29) Hong, J.; Bae, J.-H.; Jo, H.; Park, H.-Y.; Lee, S.; Hong, S. J.; Chun, H.; Cho, M. K.; Kim, J.; Kim, J.; et al. Metastable hexagonal close-packed palladium hydride in liquid cell TEM. *Nature* **2022**, *603* (7902), 631–636.
- (30) Ianiro, A.; Wu, H.; van Rijt, M. M. J.; Vena, M. P.; Keizer, A. D. A.; Esteves, A. C. C.; Tuinier, R.; Friedrich, H.; Sommerdijk, N. A. J. M.; Patterson, J. P. Liquid—liquid phase separation during amphiphilic self-assembly. *Nat. Chem.* **2019**, *11* (4), 320—328.
- (31) Mehdi, B. L.; Stevens, A.; Qian, J.; Park, C.; Xu, W.; Henderson, W. A.; Zhang, J.-G.; Mueller, K. T.; Browning, N. D. The Impact of Li Grain Size on Coulombic Efficiency in Li Batteries. *Sci. Rep* **2016**, *6* (1), 34267.
- (32) Arán-Ais, R. M.; Rizo, R.; Grosse, P.; Algara-Siller, G.; Dembélé, K.; Plodinec, M.; Lunkenbein, T.; Chee, S. W.; Cuenya, B. R. Imaging electrochemically synthesized Cu2O cubes and their morphological evolution under conditions relevant to CO2 electroreduction. *Nat. Commun.* **2020**, *11*(1) DOI: 10.1038/s41467-020-17220-6.
- (33) Williamson, M. J.; Tromp, R. M.; Vereecken, P. M.; Hull, R.; Ross, F. M. Dynamic microscopy of nanoscale cluster growth at the solid—liquid interface. *Nat. Mater.* **2003**, *2* (8), 532–536.
- (34) Sun, M.; Liao, H.-G.; Niu, K.; Zheng, H. Structural and Morphological Evolution of Lead Dendrites during Electrochemical Migration. *Sci. Rep* **2013**, 3(1) DOI: 10.1038/srep03227.
- (35) Schneider, N. M.; Park, J. H.; Grogan, J. M.; Steingart, D. A.; Bau, H. H.; Ross, F. M. Nanoscale evolution of interface morphology during electrodeposition. *Nat. Commun.* **2017**, *8*(1) DOI: 10.1038/s41467-017-02364-9.
- (36) Wang, X.; Klingan, K.; Klingenhof, M.; Möller, T.; Ferreira De Araújo, J.; Martens, I.; Bagger, A.; Jiang, S.; Rossmeisl, J.; Dau, H.; Strasser, P. Morphology and mechanism of highly selective Cu(II) oxide nanosheet catalysts for carbon dioxide electroreduction. *Nat. Commun.* **2021**, *12*(1) DOI: 10.1038/s41467-021-20961-7.
- (37) Subramanian, V.; Martin, D. C. Direct Observation of Liquid-to-Solid Phase Transformations during the Electrochemical Deposition of Poly(3,4-ethylenedioxythiophene) (PEDOT) by Liquid-Phase Transmission Electron Microscopy (LPTEM). *Macromolecules* **2021**, *54* (14), 6956–6967.
- (38) Layla Mehdi, B.; Gu, M.; Parent, L. R.; Xu, W.; Nasybulin, E. N.; Chen, X.; Unocic, R. R.; Xu, P.; Welch, D. A.; Abellan, P.; et al. In-Situ Electrochemical Transmission Electron Microscopy for Battery Research. *Microscopy and Microanalysis* **2014**, 20 (2), 484–492.
- (39) Mehdi, B. L.; Qian, J.; Nasybulin, E.; Park, C.; Welch, D. A.; Faller, R.; Mehta, H.; Henderson, W. A.; Xu, W.; Wang, C. M.; et al. Observation and Quantification of Nanoscale Processes in Lithium Batteries by Operando Electrochemical (S)TEM. *Nano Lett.* **2015**, *15* (3), 2168–2173.

- (40) Vratsanos, M. A.; Gianneschi, N. C. Direct Observation of Emulsion Morphology, Dynamics, and Demulsification. *ACS Nano* **2022**, *16* (5), 7783–7793.
- (41) Ogden, W. A.; Guan, Z. Redox Chemical-Fueled Dissipative Self-Assembly of Active Materials. *ChemSystemsChem.* **2020**, DOI: 10.1002/syst.201900030.
- (42) Van Omme, J. T.; Wu, H.; Sun, H.; Beker, A. F.; Lemang, M.; Spruit, R. G.; Maddala, S. P.; Rakowski, A.; Friedrich, H.; Patterson, J. P.; Pérez Garza, H. H. Liquid phase transmission electron microscopy with flow and temperature control. *Journal of Materials Chemistry C* **2020**, *8*, 10781.
- (43) Rizvi, A.; Mulvey, J. T.; Carpenter, B. P.; Talosig, R.; Patterson, J. P. A Close Look at Molecular Self-Assembly with the Transmission Electron Microscope. *Chem. Rev.* **2021**, *121*, 14232.
- (44) Hurst, P. J.; Mulvey, J. T.; Bone, R. A.; Selmani, S.; Hudson, R. F.; Guan, Z.; Green, J. R.; Patterson, J. P. CryoEM reveals the complex self-assembly of a chemically driven disulfide hydrogel. *Chemical Science* **2024**, *15* (3), 1106–1116.
- (45) Patterson, J. P.; Abellan, P.; Denny, M. S.; Park, C.; Browning, N. D.; Cohen, S. M.; Evans, J. E.; Gianneschi, N. C. Observing the Growth of Metal—Organic Frameworks by in Situ Liquid Cell Transmission Electron Microscopy. *J. Am. Chem. Soc.* 2015, 137 (23), 7322—7328.
- (46) Kelton, K. F.; Frenkel, D. Preface: Special Topic on Nucleation: New Concepts and Discoveries. *J. Chem. Phys.* **2016**, *145* (21), 211501.
- (47) Van Rossum, S. A. P.; Tena-Solsona, M.; Van Esch, J. H.; Eelkema, R.; Boekhoven, J. Dissipative out-of-equilibrium assembly of man-made supramolecular materials. *Chem. Soc. Rev.* **2017**, *46* (18), 5519–5535.
- (48) Yao, L.; Ou, Z.; Luo, B.; Xu, C.; Chen, Q. Machine Learning to Reveal Nanoparticle Dynamics from Liquid-Phase TEM Videos. *ACS Central Science* **2020**, *6* (8), 1421–1430.
- (49) Woehl, T. J.; Park, C.; Evans, J. E.; Arslan, I.; Ristenpart, W. D.; Browning, N. D. Direct Observation of Aggregative Nanoparticle Growth: Kinetic Modeling of the Size Distribution and Growth Rate. *Nano Lett.* **2014**, *14* (1), 373–378.
- (50) Rizvi, A.; Mulvey, J. T.; Patterson, J. P. Observation of Liquid–Liquid-Phase Separation and Vesicle Spreading during Supported Bilayer Formation via Liquid-Phase Transmission Electron Microscopy. *Nano Lett.* **2021**, *21* (24), 10325–10332.
- (51) Otsu, N. A Threshold Selection Method from Gray-Level Histograms. *IEEE Transactions on Systems, Man, and Cybernetics* **1979**, 9 (1), 62–66.
- (52) Masaro, L.; Zhu, X. X. Physical models of diffusion for polymer solutions, gels and solids. *Prog. Polym. Sci.* **1999**, 24 (5), 731–775.
- (53) Wang, Z.; Bovik, A. C.; Sheikh, H. R.; Simoncelli, E. P. Image Quality Assessment: From Error Visibility to Structural Similarity. *IEEE Transactions on Image Processing* **2004**, *13* (4), 600–612.
- (54) Mulvey, J. T.; Iyer, K. P.; Ortega, T.; Merham, J. G.; Pivak, Y.; Sun, H.; Hochbaum, A. I.; Patterson, J. P. Correlating electrochemical stimulus to structural change in liquid electron microscopy videos using the structural dissimilarity metric. *Ultramicroscopy* **2024**, 257, No. 113894.